Supporting Information for Proper Thermal Equilibration of Simulations with Drude Polarizable Models: Temperature Grouped Dual-Nosé-Hoover Thermostat

Chang Yun Son,[†,‡] Jesse G. McDaniel,[†,¶] Qiang Cui,[†,§] and Arun Yethiraj[*,†]

†*Department of Chemistry and Theoretical Chemistry Institute, University of Wisconsin-Madison, 1101 University Avenue, Madison, WI 53706*

‡*Present address: Division of Chemistry and Chemical Engineering, California Institute of Technology, Pasadena, CA 91125*

¶*Present address: School of Chemistry and Biochemistry, Georgia Institute of Technology, Atlanta, GA 30332*

§*Present address: Department of Chemistry, Department of Biomedical Engineering and Department of Physics, Boston University, 590 Commonwealth Avenue, Boston, MA 02215*

E-mail: yethiraj@wisc.edu

1 Simulation protocols

For each system, a pre-equilibrated simulation box is obtained from previous works;[1–3] the systems of water, NaCl/water, acetone, and $BMIM^+BF_4^-$ consist of 4096 water molecules, 3936 water molecules and 80 ion pairs of NaCl, 1000 acetone molecules, and 200 ion pairs of $BMIM^+BF_4^-$, respectively. Each simulation involves an energy minimization step, a 6-11 ns of isothermal and isobaric (NPT) simulation step, and an 11-51 ns of isothermal (NVT) simulation step. Both particle positions and velocities are saved every picosecond in all simulations for analysis. The system densities are calculated with the NPT simulation and the translational diffusion coefficients and effective temperatures are calculated with the NVT simulations. The first nanosecond of each NVT/NPT simulation is excluded from the analysis.

The temperatures associated with nuclear (real) DOF (T) and polarization (Drude) DOF (T^*) are set with dual-temperature thermostats. The T is set to 298 K except for $BMIM^+BF_4^-$, which is simulated at a higher temperature (400 K) to overcome the slow dynamics due to its high viscosity. The T^* is set to 1 K for all systems. For NPT simulations, a Monte Carlo barostat is used to keep the system pressure at 1 bar. One femtosecond time step is used in all simulations to ensure stable integration with the high frequency Drude motions. Electrostatics are treated with the particle mesh Ewald (PME) method[4] and the van der Waals interactions are cut off at 1.0 nm for water and NaCl/water, and at 1.4 nm for acetone and $BMIM^+BF_4^-$. Water molecules are treated as completely rigid, and bonds containing hydrogen (C-H) are constrained in other molecules. For acetone, we also compare simulations with different constraints. We note that, in the original study of McDaniel et al.,[2] acetone was treated as completely rigid to eliminate any intramolecular DOF.

To benchmark the effect of the different thermostat schemes on the predicted properties, simulations are performed with a broad set of thermostat parameters. For each system, a large set of combinations for the characteristic time scales τ and τ^* are tested for all three thermostat schemes (dual-LV, dual-NH and tgNH thermostats), and the effect of using bond

constraints as well as using Nosé-Hoover chain (with a chain of 10 thermostats) vs. no chain are tested for both the dual-NH thermostat and the tgNH thermostat.

Translational diffusion coefficients are calculated from the NVT simulations using the Einstein relation,

$$D = \lim_{t\to\infty} \frac{1}{6} \frac{\partial < |\mathbf{R_{CM},}_i(t) - \mathbf{R_{CM},}_i(0)|^2 >}{\partial t}. \tag{S1}$$

Each NVT trajectory is divided into five blocks excluding the first nanosecond, and the diffusion coefficients are calculated from the slope of mean square displacement vs. time for the time range up to the half of the block length (0-1 ns for water, NaCl/water and acetone, and 0-5 ns for $BMIM^+BF_4^-$). When the system size is small, the calculated diffusion coefficient needs to be corrected for finite box size effect,[5]

$$D_0 = D_{PBC} + 2.837297 \frac{k_B T}{6\pi\eta L} \tag{S2}$$

where D_0 is the true diffusion coefficient of the infinite system, D_{PBC} is the diffusion coefficient calculated using periodic boundary conditions with a cubic box dimension L, and η represents the shear viscosity of the solvent. This finite size correction is used to compare our estimated diffusion coefficients with the literature data in all systems. To minimize the uncertainty and fluctuations in the value of the viscosity in Eq. S2 due to thermostat choices, we use experimentally measured viscosity at the desired temperature. We note the SCF results in literature for SWM4-NDP water and SAPT-FF acetone contained significant finite-size-error due to much smaller system size than studied here; 250 water molecules and $\sim$ 130 acetone molecules were used to parametrize the models. Finite-size-corrected diffusion constant of SWM4-NDP water has been reported previously,[6] which is higher than the value reported here (2.85 vs. 2.68 $\times 10^{-5} cm^2/s$) due to the use of simulated value of viscosity (0.66 cP) as oppose to the experimental value (0.89 cP) used in this work. For non-aqueous systems, the system densities are found to be strongly dependent on the thermostat scheme (except for the tgNH thermostat), which in turn affects the diffusion coefficients significantly.

To separate the two effects of the thermostat on the predicted dynamics, we perform the NVT simulations both at the experimental density and at the predicted density with the thermostat used.

2 Effect of thermostat coupling strength

We test a large set of combinations of thermostat parameters, including the heat bath coupling times τ and τ^*, different extent of constraints, NPT vs. NVT simulations at the experimental density, as well as the use of Nosé-Hoover chain variables. SI table S1 summarize the combinations tested to gather pressure-temperature data presented in main Figure 3. In SI Figures S1-S4, the effects of thermostat on density and effective temperatures are presented with different coupling strengths.

Table S1: Combination of thermostat coupling strengths τ and τ^* tested in this study. Combined with other parameters, 40 $\sim$ 130 independent simulations are performed for each of the four systems.

τ (ps)	10	10	1	1	1	1	0.1	0.1	0.1
τ^* (ps)	10	1	10	1	0.1	0.05	1	0.1	0.005

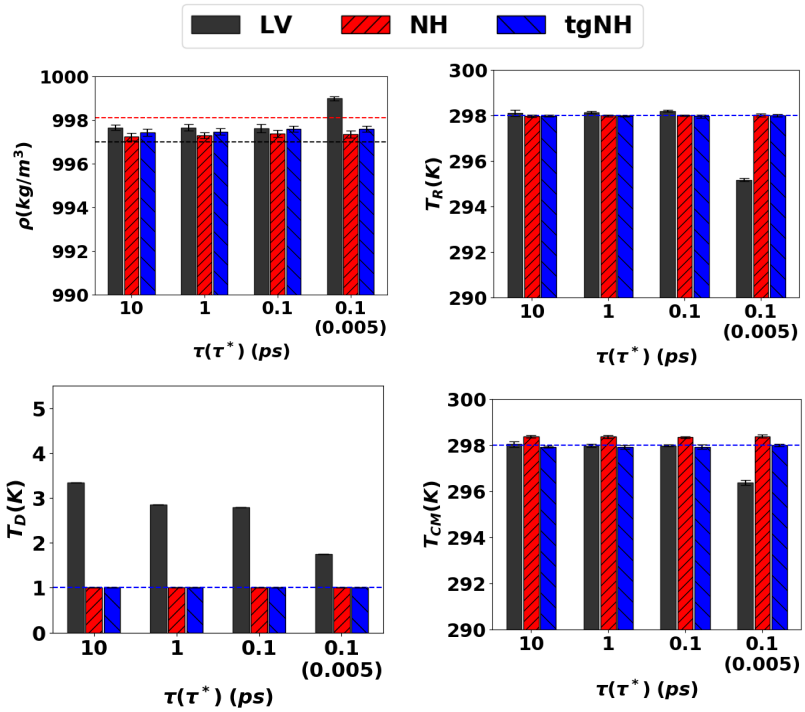

Figure S1: Predicted properties of water at 25 ^oC, analogous to Figure 2 in main text; black dotted line: experimental density; red dotted line: density predicted with SCF scheme; blue dotted line: set temperatures T and T^*.

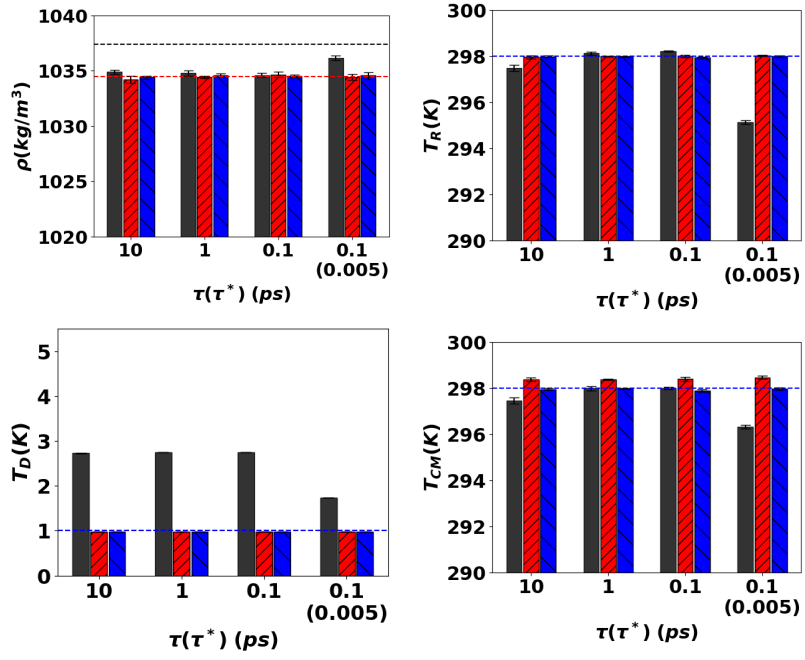

Figure S2: Predicted static properties of 1M $NaCl_{(aq)}$ at 25 ^oC, analogous to SI Figure S1. Experimental density of 1M $NaCl_{(aq)}$ at 25 ^oC is from ref.[7]

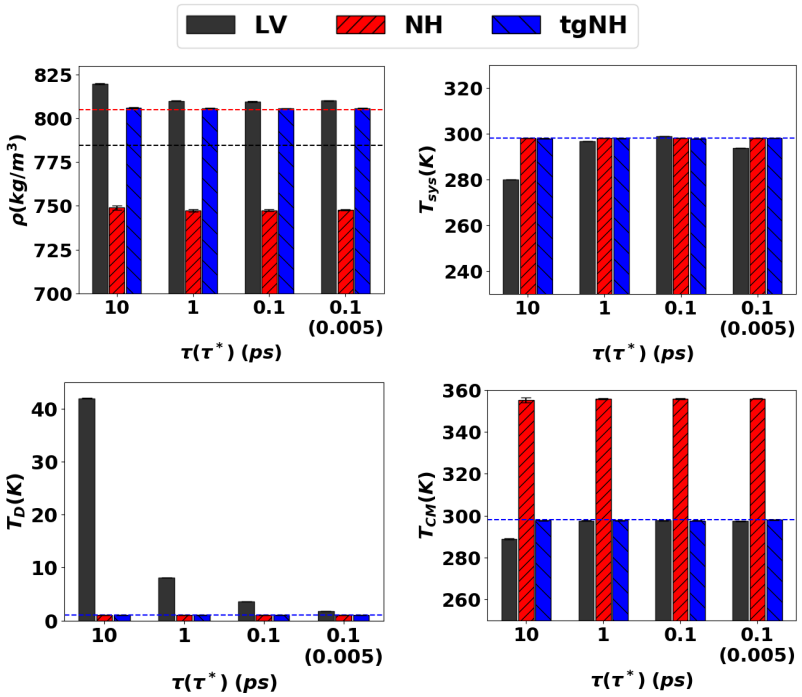

Figure S3: Predicted static properties of acetone at 25 ^oC, analogous to SI Figure S1.

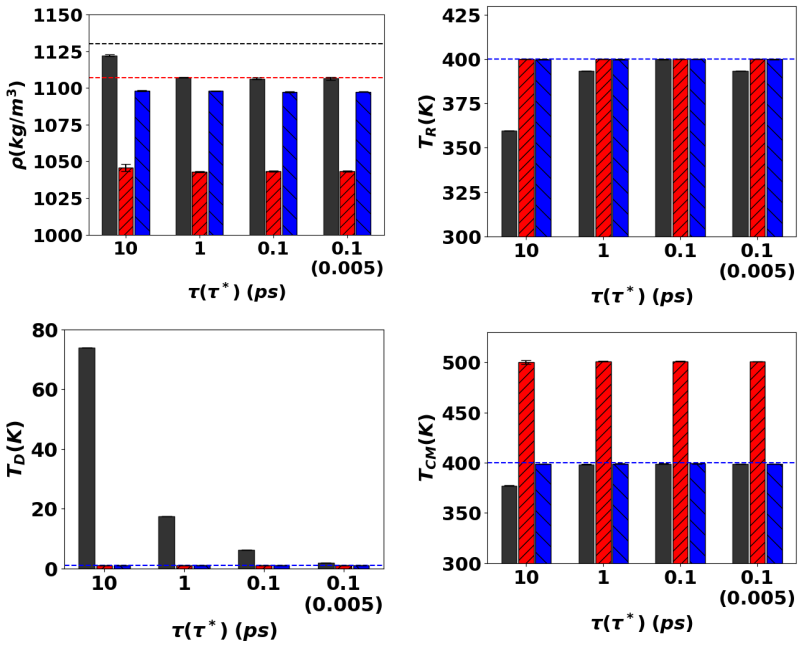

Figure S4: Predicted static properties of $BMIM^+BF_4^-$ at 400 K, analogous to SI Figure S1.

3 Effect of bond constraints

In Figures S5 and S6, we examine the effect of using different bond constraints for acetone; simulations using no bond constraints (NB), constraining C-H bonds (HB), and constraining all bonds (All) with the dual-NH thermostat are compared with the tgNH thermostat using HB constraints. All simulations are performed at the experimental density to minimize the effect of density differences with the thermostat schemes. Constraining all bonds produces the least deviation from simulations with the SCF scheme and the results of the tgNH thermostat. On the other hand, constraining no bonds leads to extreme deviations; D is more than two times larger than SCF and tgNH thermostat results, T_{CM} reaches 250 K higher than the set temperature T while both $T_{C_0}^{int}$ and $T_{CH_3}^{int}$ are 40 K lower than T. By constraining bonds including hydrogen atoms (HB constraint), many of such deviations get reduced, where T_{CM} is about only 50 K higher than T and both $T_{CH_3}^{int}$ and T_{O}^{int} are closer to T (less than 10 K deviation). This is because the high frequency C-H stretching motions strongly couple to the Drude oscillators and lose much of the kinetic energy. As discussed in the main text, the central C_0 carbon also loses much kinetic energy due to the high frequency improper dihedral and angular motion, but HB constraint cannot alleviate this mode, resulting in similar $T_{C_0}^{int}$ for all three NH-NB, NH-HB, tgNH-HB cases. Intramolecular effective temperatures of atom groups are not shown for the simulations with all bond constraint, since the constraints couple the intramolecular degrees of freedom of all the atoms and separating atom group temperature is not straightforward. We emphasize that the particular value of bond strength may vary between different force fields, thus the fact that predictions of bulk thermodynamic properties and effective temperature of the system may depend on the specifics of intramolecular parameters is provocative. This analysis serves as a great example highlighting the importance of proper thermalization, especially for CM DOF.

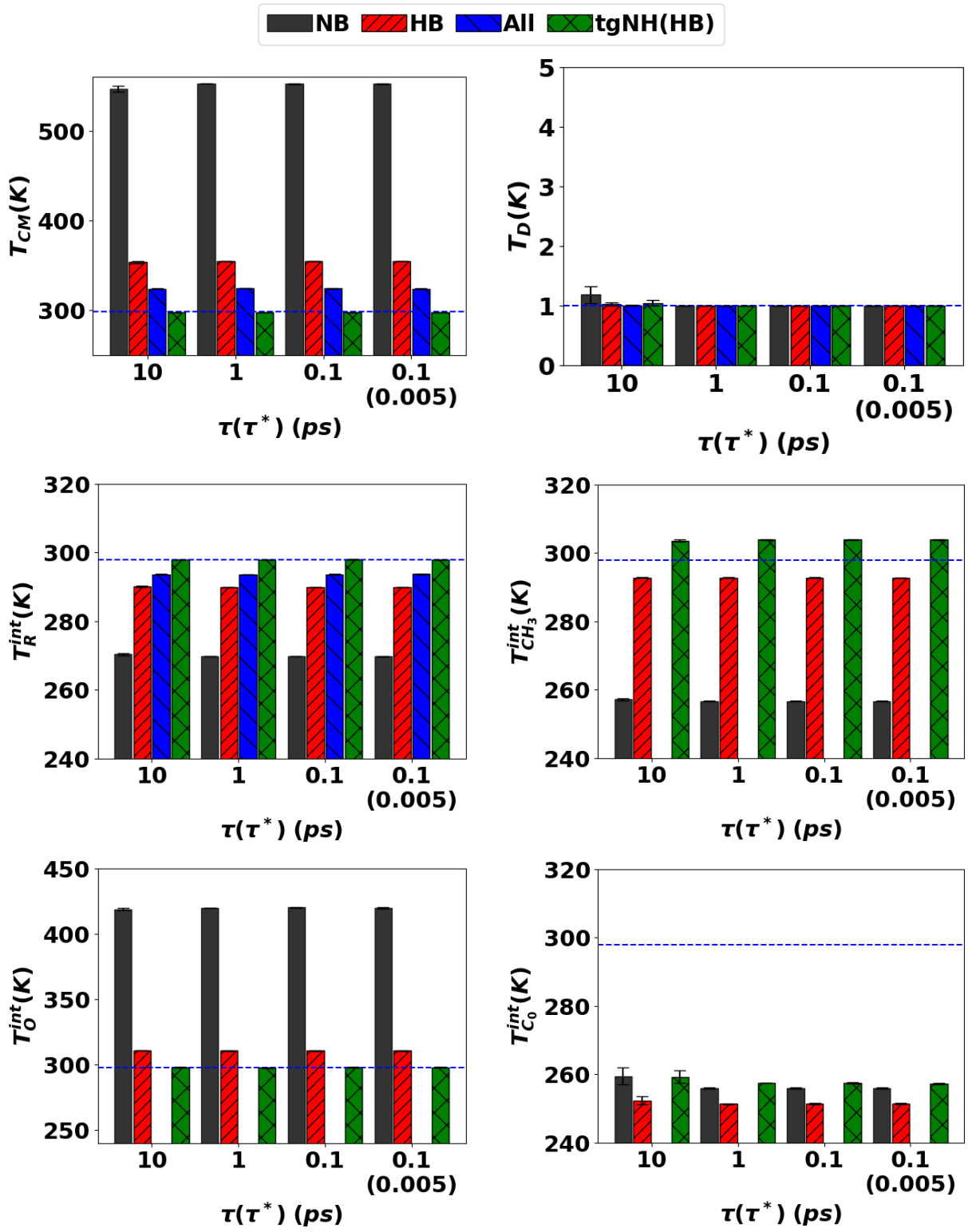

Figure S5: Effect of bond constraints on the effective temperature representing intramolecular (int) motions associated with different atoms in acetone. Effective temperatures are analogous to Figure 4 in the main text. The blue dotted line shows the set temperature of 298 K.

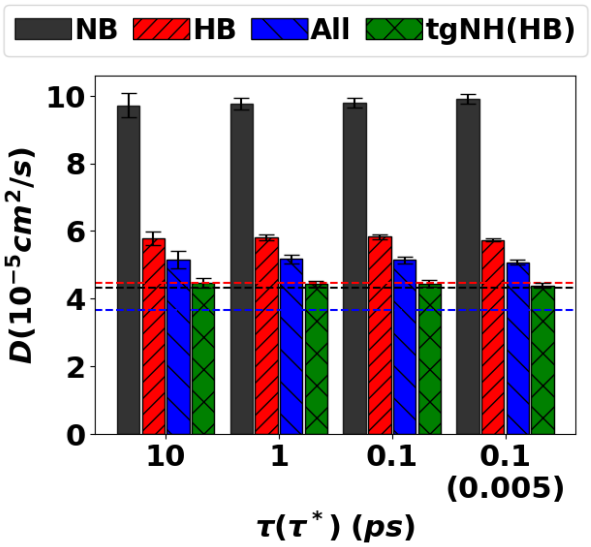

Figure S6: Effect of bond constraints on the calculated self-diffusion coefficient (D) of acetone with the dual-NH thermostat. Simulations are performed at the experimental density of acetone (784 kg/m^3).[8] Black: no bond constraint is used (NB), red: C-H bonds are constrained (HB), blue: all bonds are constrained (All), green: tgNH thermostat with HB constraints (tgNH(HB)). Simulations with the tgNH thermostat and constraints for all bonds (tgNH(All)) are very similar to the tgNH(HB) case. Black horizontal lines: experimental values.,[8] blue horizontal lines: Literature D values calculated with the SCF scheme,[2] red horizontal lines: finite size correction[5] is added to the SCF values.

4 Intramolecular effective temperatures in $BMIM^+BF_4^-$

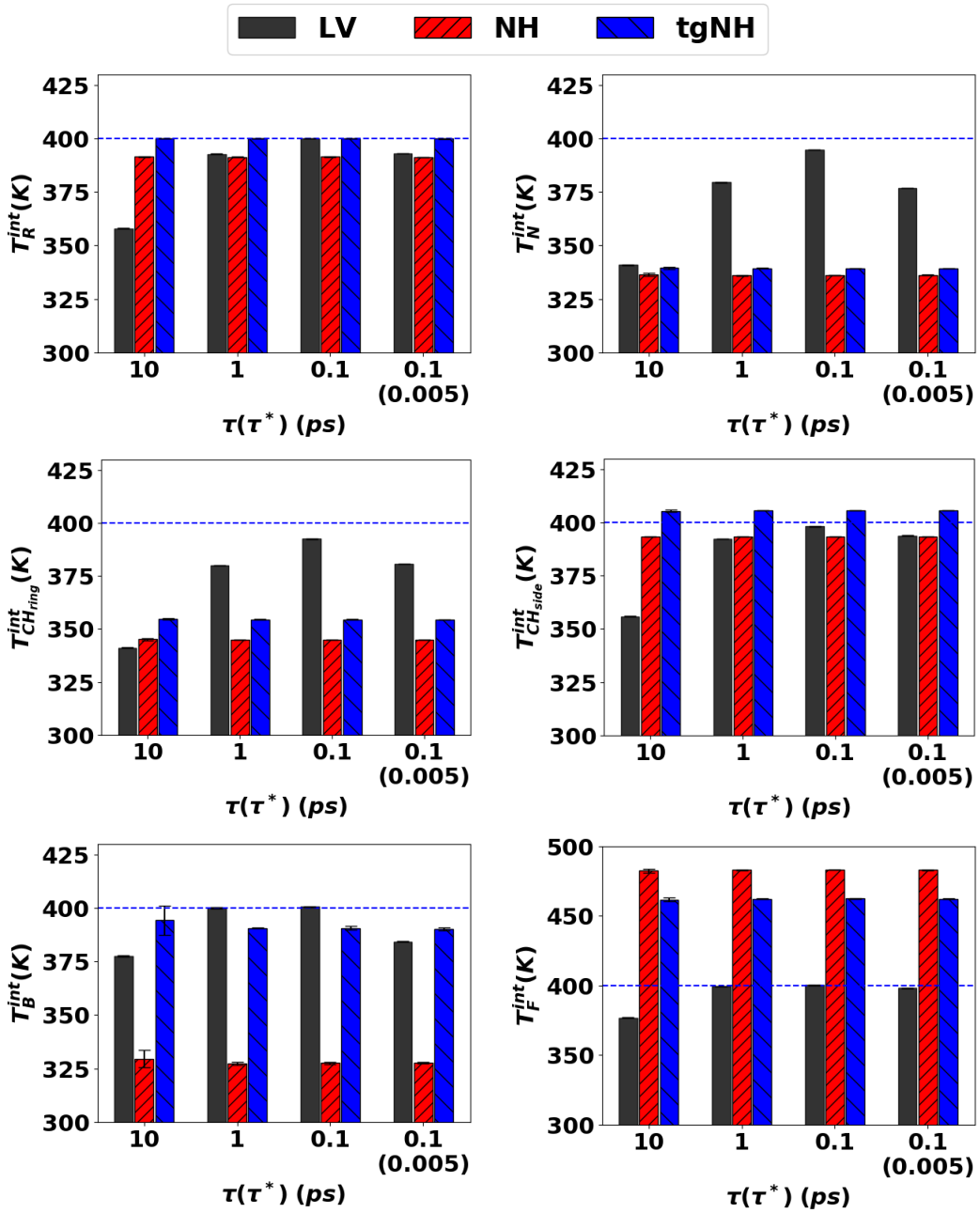

Figure S7: The effect of the thermostats on the effective temperature representing intramolecular (int) motions associated with different atoms in $BMIM^+BF_4^-$. T_R^{int}: temperature of total intramolecular real particles DOF; T_N^{int}: temperature of ring N atoms; $T_{CH_{ring}}^{int}$: temperature of ring CH groups; $T_{CH_{side}}^{int}$: temperature of the methyl and butyl groups; T_B^{int}: temperature of the central boron atoms of the anion; T_F^{int}: temperature of the fluorine atoms of the anion. The blue dotted line shows the set temperature of 400 K. Both T_N^{int} and $T_{CH_{ring}}^{int}$ lose most kinetic energy to the Drude DOF, while T_{CM} and T_F (which does not involve any high frequency mode) gains most kinetic energy.

5 Effect of using Nosé-Hoover chain

In non-polarizable systems, using Nosé-Hoover chain variation of NH thermostat improves the ergodicity of the dynamics. In this section, we compare the effect of including chain variables for dual-NH (NHC) and tgNH (tgNHC) thermostats. In dual thermostat scheme, one can use chain variables either for both real and Drude DOF, or just for the real DOF. Thus we compare two different Nosé-Hoover chain schemes per thermostat, namely dual-NH with chain for both DOF (NHC), dual-NH with chain for only real DOF (NHCreal), tgNH with chain for both DOF (tgNHC), tgNH with chain for only real DOF (tgNHCreal). All simulations with chain variables use 10 chains for each DOF.

As shown in Figures S8 and S9, none of the tested schemes of including chain variables improve the thermostat performance. The predicted system properties are strongly dependent on the coupling to the heat bath, and weak coupling ($\tau = \tau^* = 10ps$) leads to significant deviation from the predictions of either dual-NH or tgNH thermostat. In general, using chain variables in thermostat weakens the coupling to heat bath, thus NHC-based thermostats require stronger coupling to heat bath to achieve the same amount of heat transfer between the bath and the system. Figures S8 and S9 show thermostats with chain variables require moderate to strong coupling to heat bath ($\tau = \tau^* < 1ps$), and does not improve equipartitioning even with a strong coupling to heat bath; both NHC and NHCreal with $\tau = 0.1ps$ are consistent with dual-NH thermostat results, and tgNHC and tgNHCreal with $\tau = 0.1ps$ are consistent with tgNH thermostat results.

Another observation is that using chain variables for both real and Drude DOF fails to equilibrate the Drude temperature T_D at 1 K, similar to the case of dual-LV thermostat. Both NHC and tgNHC schemes show Drude temperature T_D as high as 35 K, while both NHCreal and tgNHCreal schemes maintain T_D at the set temperature of $T^* = 1K$. Based on these observations, we conclude that one should not use chain variables for Drude simulations with the dual-NH or tgNH thermostats.

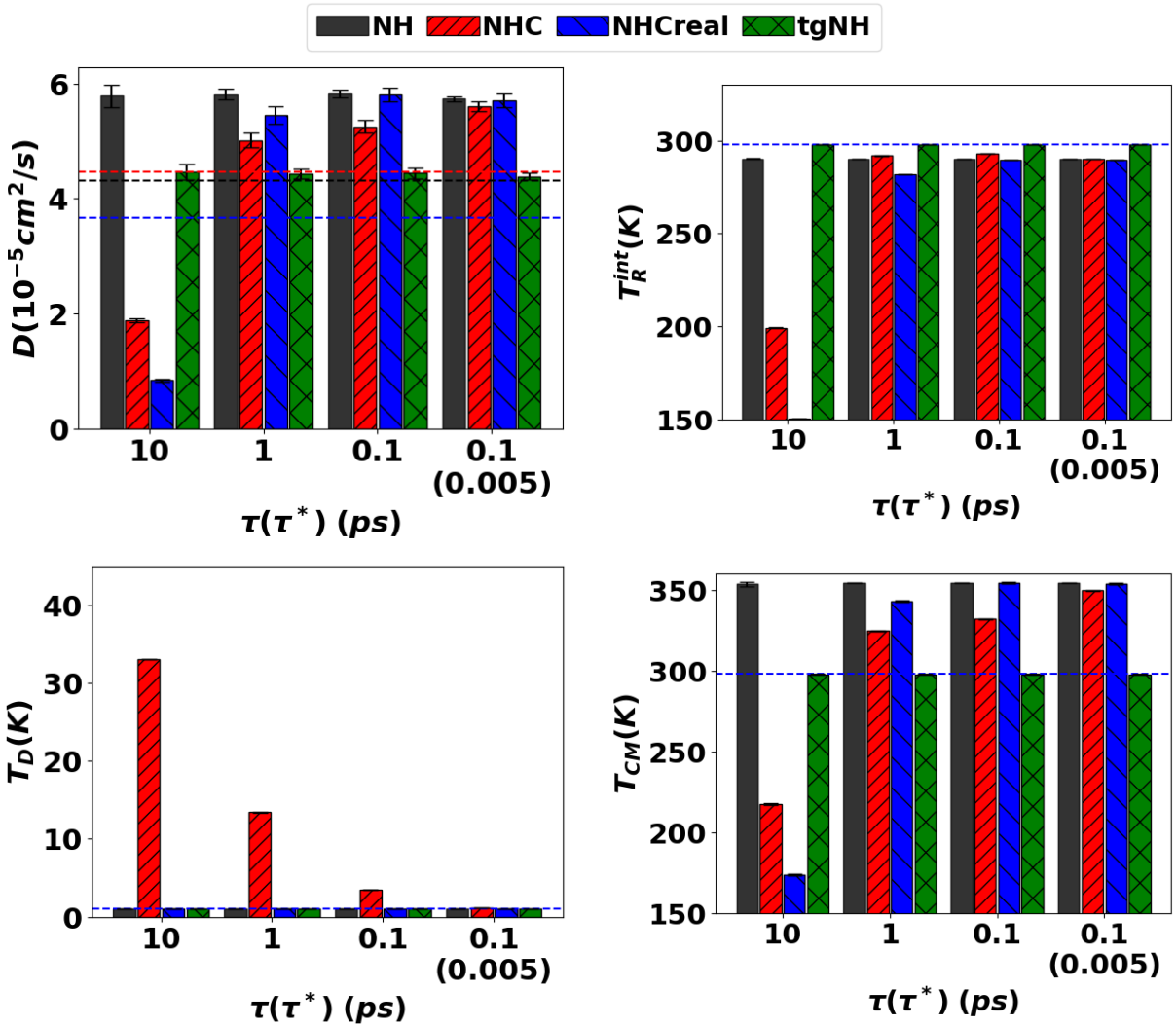

Figure S8: Effect of using Nosé-Hoover chain for dual-NH thermostat. NHC: Nosé-Hoover chain for both real and Drude DOF; NHCreal: Nosé-Hoover chain for real DOF only. Effective temperatures and dotted reference values are analogous to Figures S5 and S6

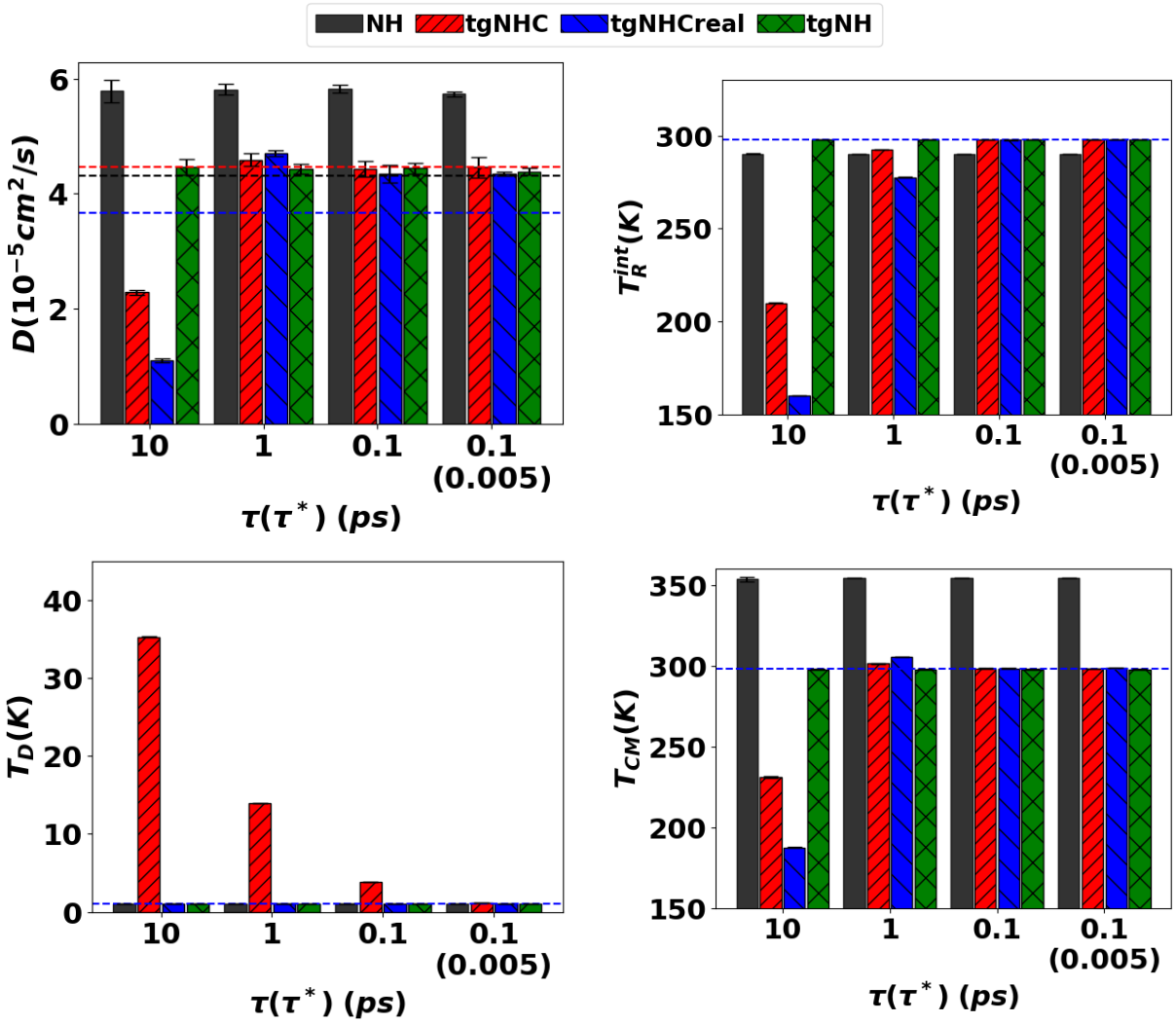

Figure S9: Effect of using Nosé-Hoover chain for tgNH thermostat. tgNHC: Nosé-Hoover chain for both real and Drude DOF; tgNHCreal: Nosé-Hoover chain for real DOF only. Effective temperatures and dotted reference values are analogous to Figures S5 and S6

6 Dual-CSVR thermostat

In classcial MD simulations with non-polarizable FFs, the canonical sampling through velocity rescaling (CSVR) thermostat developed by Parrinello *et al.*[9] is shown to have good control of the system temperature while preserving canonical distribution of kinetic energies without affecting the dynamic properties. To the best of our knowledge, CSVR thermostat has not been implemented with dual-temperature scheme for simulations with polarizable FFs in the literature. To test the effect of dual-CSVR thermostat, we have implemented dual-CSVR thermostat in the simulation package OpenMM as following. In the dual-CSVR thermostat, the equations of motion for the particles are simple Newtonian dynamics. After each timestep, the velocities of real DOF and Drude DOF are scaled by scaling factors α and α^*, respectively; the scaling factors are determined to satisfy canonical ensemble such that,

$$\alpha^2 = e^{-\Delta t/\tau} + \frac{\bar{K}}{N_f K}(1 - e^{-\Delta t/\tau}) \left(R_1^2 + \sum_{i=2}^{N_f} R_i^2 \right) + 2e^{-\Delta t/2\tau} \sqrt{\frac{\bar{K}}{N_f K}(1 - e^{-\Delta t/\tau})} R_1, \quad \text{(S3)}$$

$$\alpha^{*2} = e^{-\Delta t^*/\tau^*} + \frac{\bar{K^*}}{N_f^* K^*}(1 - e^{-\Delta t^*/\tau^*}) \left(R_1^{*2} + \sum_{i=2}^{N_f^*} R_i^{*2} \right) + 2e^{-\Delta t^*/2\tau^*} \sqrt{\frac{\bar{K^*}}{N_f^* K^*}(1 - e^{-\Delta t^*/\tau^*})} R_1^*, \quad \text{(S4)}$$

where R_1, R_i, R_1^*, R_i^* are independent random numbers from a Gaussian distribution with unitary variance. As previous, $N_f = 3N - n_c$ and $N_f^* = 3N_D$ represent number of real and Drude DOF, respectively; τ and τ^* are coupling relaxation time for real and Drude DOF; $\bar{K} = N_f k_B T/2$ and $\bar{K^*} = N_f^* k_B T/2$ are desired kinetic energies for real and Drude DOF; K, K^* are calculated kinetic energies for real and Drude DOF; Δt and Δt^* the timestep for real and Drude DOF; we perform multiple timestep iteration (20 used here) of velocity update for Drude DOF per each real DOF velocity update and position update.

Figure S10 shows th effect of using dual-CSVR thermostat on the dynamics and static properties of acetone. Interestingly, dual-CSVR thermostat shows artifacts of both dual-

LV and dual-NH thermostat. Similar to the dual-NH thermostat, the predicted diffusion coefficients are strongly overestimated, and the effective temperature of CM DOF (T_{CM}) is higher than the set temperature. Furthermore, similar to dual-LV thermostat, the effective Drude temperature T_D does not settle at the low temperature (1 K), indicating significant heat flow from real DOF is not compensated by the thermostat. Stronger coupling for Drude DOF alleviates the problem of high Drude temperature, but the system still suffers from incorrect CM translational temperature which results in a prediction where the density is too low and the diffusion coefficient is too high. This analysis clearly indicates the incorrect T_{CM} is a general problem in velocity rescaling thermostat. Furthermore, combined with the previous discussions on the dual-NHC thermostat, we speculate non-ergodic character of dual-NH thermostat actually helps the stabilization of Drude temperature. We expect using CM temperature group and strong coupling for Drude DOF with CSVR thermostat would also provide accurate description of the thermodynamic properties similar to tgNH thermostat, but we suggest tgNH thermostat is a preferred choice of thermostat due to the robust temperature control (especially for the Drude temperature).

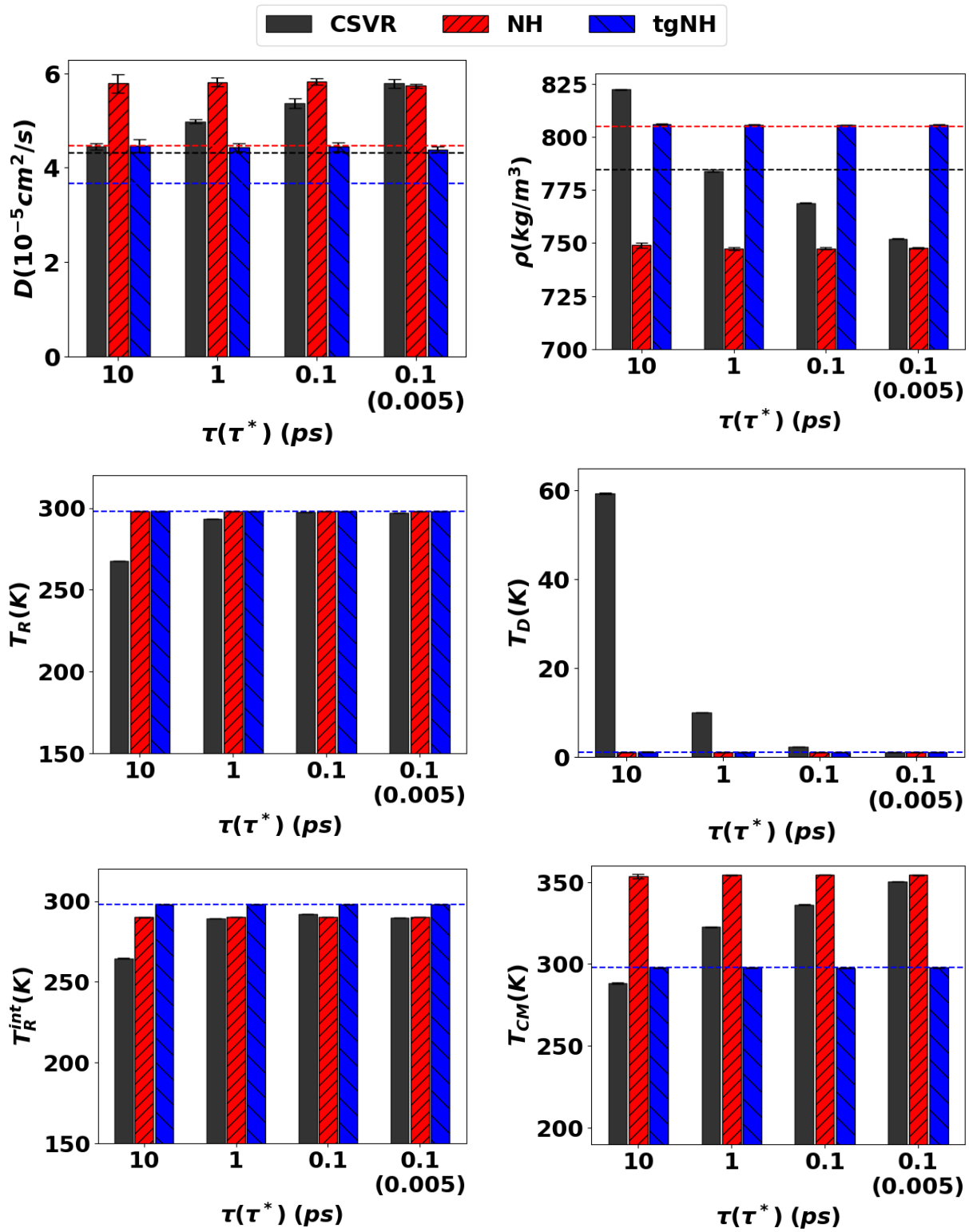

Figure S10: Effect of dual-CSVR thermostat analogous to Figures 1, 2 and 4 in main text. Black: dual-CSVR thermostat; red: dual-NH thermostat; blue: tgNH thermostat. Diffusion coefficients and effective temperatures are calculated from NVT simulation at experimental density, while density is calculated from NPT simulation.

7 Other thermodynamic properties

In this section, we examine the effect of thermostat on the predicted rotational relaxation time (τ_{rot}) and static dielectric constant (ϵ) of acetone at 298 K. Simulations are performed at experimental density of acetone with HB constraint. τ_{rot} is calculated by fitting the rotational auto correlation function $< \sum_i \mu_i(0) \cdot \mu_i(t) > / < \sum_i \mu_i^2 >$ to a single exponential $\exp(-t/\tau_{rot})$, where $\mu_i(t)$ is the dipole moment of each molecule. The static dielectric constant is calculated from fluctuations of the total system dipole moment ($\mathbf{M}$),

$$\epsilon = 1 + \frac{4\pi}{3k_B TV} \left(< \mathbf{M}^2 > - < \mathbf{M} >^2 \right). \tag{S5}$$

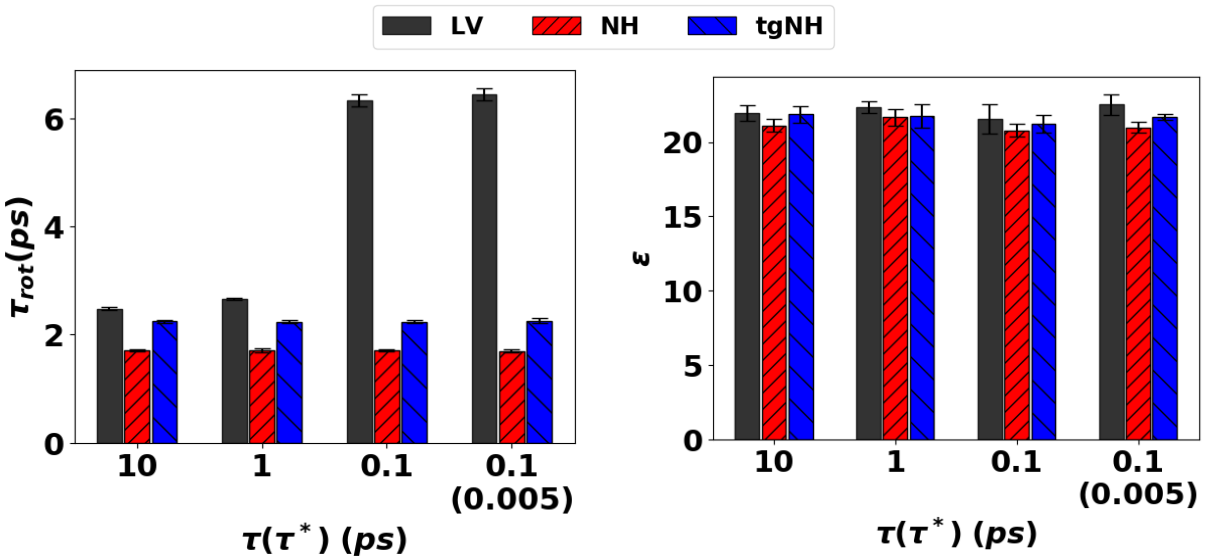

Figure S11: Effect of thermostat on the calculated rotational relaxation time (τ_{rot}) and static dielectric constant (ϵ) of acetone at 298 K.

As shown in Figure S11, the dual-LV thermostat systematically retards the rotational diffusion of the molecules, as indicated by the increasing τ_{rot} with increasing coupling strength. This is consistent with the trend in translational diffusion, and the same trend was observed with single LV thermostat for nonpolarizable simulations.[10] On the other hand, simulations with the dual-NH thermostat underestimates the rotational relaxation time (faster rotational diffusion) compared to the tgNH thermostat, indicating effective rotational temperature be-

ing higher than the set temperature.

The calculated static dielectric constant is relatively insensitive to the choice of the thermostat scheme or the strength of the coupling to heat baths. This can be understood from the consideration that the static dielectric constant is only dependent on the fluctuations of the system dipole, which are captured correctly as long as the structural ensemble is properly represented. Since the simulations are performed at the same experimental density, all the tested thermostats sample the proper structural ensemble at sufficiently long simulation time.

8 Simulation Performance

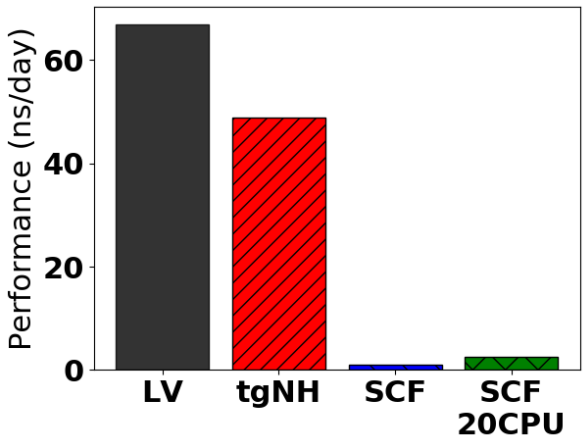

Figure S12: Benchmark of simulation performance with different thermostat schemes for system containing 1000 acetone molecules. We note dual-NH thermostat shows identical performance to tgNH thermostat (within $1 \sim 2$ ns/day difference) and thus is not shown in the figure. dual-LV, dual-NH, tgNH, SCF simulations are performed with OpenMM version 7.2 in mixed precision, utilizing single NVIDIA Titan-XP GPU with single core of Intel(R) Core(TM) i7-7700 3.60GHz CPU. SCF-20CPU simulation is performed with GROMACS version 4.6.5 in single precision, utilizing 20 cores of Intel(R) Xeon(R) 2.20GHz CPU E5-2630 v4 processors. SCF scheme with GPU performs less than 1 ns/day, and SCF-20CPU with single precision performs ~ 2.3 ns/day. We note dual-NH thermostat implemented in GROMACS performed about four times faster than SCF scheme in CPU.[11]

References

(1) Kim, J. S.; Wu, Z.; Morrow, A. R.; Yethiraj, A.; Yethiraj, A. Self-diffusion and viscosity in electrolyte solutions. *J. Phys. Chem. B* **2012**, *116*, 12007–12013.

(2) McDaniel, J. G.; Schmidt, J. R. First-principles many-body force fields from the gas phase to liquid: A "universal" approach. *J. Phys. Chem. B* **2014**, *118*, 8042–8053.

(3) Son, C. Y.; McDaniel, J. G.; Schmidt, J. R.; Cui, Q.; Yethiraj, A. First-Principles United Atom Force Field for the Ionic Liquid $BMIM^{+}BF_{4}^{-}$: An Alternative to Charge Scaling. *J. Phys. Chem. B* **2016**, *120*, 3560–3568.

(4) Darden, T.; York, D.; Pedersen, L. Particle Mesh Ewald: An Nlog(N) Method for Ewald Sums in Large Systems. *J. Chem. Phys.* **1993**, *98*, 10089–10092.

(5) Yeh, I. C.; Hummer, G. System-size dependence of diffusion coefficients and viscosities from molecular dynamics simulations with periodic boundary conditions. *J. Phys. Chem. B* **2004**, *108*, 15873–15879.

(6) Yu, W.; Lopes, P. E. M.; Roux, B.; MacKerell, A. D. Six-site Polarizable Model of Water Based on the Classical Drude Oscillator. *J. Chem. Phys.* **2013**, *138*, 034508.

(7) Pitzer, K. S.; Peiper, J. C.; Busey, R. H. Thermodynamic Properties of Aqueous Sodium Chloride Solutions. *J. Phys. Chem. Ref. Data* **1984**, *13*, 1.

(8) Ahn, C. B.; Lee, S. Y.; Nalcioglu, O.; Cho, Z. H. An improved nuclear magnetic resonance diffusion coefficient imaging method using an optimized pulse sequence. *Med. Phys.* **1986**, *13*, 789–793.

(9) Bussi, G.; Donadio, D.; Parrinello, M. Canonical sampling through velocity rescaling. *J. Chem. Phys.* **2007**, *126*, 014101.

(10) Basconi, J. E.; Shirts, M. R. Effects of temperature control algorithms on transport properties and kinetics in molecular dynamics simulations. *J. Chem. Theory Comput.* **2013**, *9*, 2887–2899.

(11) Lemkul, J. A.; Roux, B.; van der Spoel, D.; MacKerell, A. D. Implementation of Extended Lagrangian Dynamics in GROMACS for Polarizable Simulations Using the Classical Drude Oscillator Model. *J. Comput. Chem.* **2015**, *36*, 1473–1479.